REPORT DOCUMENTATION PAGE

Form Approved
OMB No. 0704-0188

Public reporting burden for this collection of information is estimated to average 1 hour per response, including the time for reviewing instructions, searching existing data sources, gathering and maintaining the data needed, and completing and reviewing the collection of information. Send comments regarding this burden estimate or any other aspect of this collection of information, including suggestions for reducing this burden, to Washington Headquarters Services, Directorate for Information Operations and Reports, 1215 Jefferson Davis Highway, Suite 1204, Arlington, VA 22202-4302, and to the Office of Management and Budget, Paperwork Reduction Project (0704-0188), Washington, DC 20503.

1. AGENCY USE ONLY *(Leave blank)*	2. REPORT DATE	3. REPORT TYPE AND DATES COVERED
	31.Jan.03	THESIS

4. TITLE AND SUBTITLE
COMPARING TRMM RAINFALL RETRIEVAL WITH NOAA BUOY RAIN GAUGE DATA

5. FUNDING NUMBERS

6. AUTHOR(S)
1ST LT PHILLIPS AMY B

7. PERFORMING ORGANIZATION NAME(S) AND ADDRESS(ES)
TEXAS A&M UNIVERSITY

8. PERFORMING ORGANIZATION REPORT NUMBER
CI02-847

9. SPONSORING/MONITORING AGENCY NAME(S) AND ADDRESS(ES)
THE DEPARTMENT OF THE AIR FORCE
AFIT/CIA, BLDG 125
2950 P STREET
WPAFB OH 45433

10. SPONSORING/MONITORING AGENCY REPORT NUMBER

11. SUPPLEMENTARY NOTES

12a. DISTRIBUTION AVAILABILITY STATEMENT
Unlimited distribution
In Accordance With AFI 35-205/AFIT Sup 1

12b. DISTRIBUTION CODE

13. ABSTRACT *(Maximum 200 words)*

DISTRIBUTION STATEMENT A
Approved for Public Release
Distribution Unlimited

20030221 174

14. SUBJECT TERMS	15. NUMBER OF PAGES
	47
	16. PRICE CODE

17. SECURITY CLASSIFICATION OF REPORT	18. SECURITY CLASSIFICATION OF THIS PAGE	19. SECURITY CLASSIFICATION OF ABSTRACT	20. LIMITATION OF ABSTRACT

The views expressed in this article are those of the author and do not reflect the official policy of position of the United States Air Force, Department of Defense, of the U.S. Government.

COMPARING TRMM RAINFALL RETRIEVAL WITH NOAA BUOY RAIN GAUGE DATA

AMY BLACKMORE PHILLIPS
Capt, USAF
2002
47 pages
M.S. Atmospheric Sciences
Texas A&M University

REFERENCES

Chang, A. T. C. , L. S. Chiu, and T. T. Wilheit, 1993: Oceanic monthly rainfall derived from SSM/I. *Eos, Trans. Amer. Geophys. Union.*, **74**, 505-513.

Haddad, Z. S., E. A. Smith, C. D. Kummerow, T. Iguchi, M. R. Farrar, S. L. Durden, M. Alves, and W. S. Olson, 1997: The TRMM 'day-1' radar/radiometer combined rain-profiling algorithm. *Journal of the Meteorological Society of Japan*, **75**, 799-808.

Hitschfeld, W., and J. Bordan, 1954: Errors inherent in the radar measurement of rainfall at attenuating wavelengths. *J. Meteor.*, **11**, 58-67.

Iguchi, T., and R. Meneghini, 1994: Intercomparison of single-frequency methods for retrieving a vertical rain profile from airborne or spaceborne radar data. *J. Atmos. Oceanic Technol.*, **11**, 1507-1516.

Iguchi, T., T. Kozu, R. Meneghini, J. Awaka, K. Okamoto, 2000: Rain-profiling algorithm for the TRMM Precipitation Radar. *J. Appl. Meteor.*, **39**, 2038-2052.

Kummerow, C., 1993: On the accuracy of the Eddington approximation for radiative transfer in the microwave frequencies. *J. Geophys. Res.*, **98**, 2757-2765.

Kummerow, C., W. S. Olson, and L. Giglio, 1996: A simplified scheme for obtaining precipitation and vertical hydrometeor profiles from passive microwave sensors. *IEEE Trans. Geosci. Remote Sens.*, **34**, 1213-1232.

Kummerow, C. D., W. Barnes, T. Kozu, J. Shiue, and J. Simpson, 1998: The Tropical Rainfall Measuring Mission (TRMM) sensor package. *J. Atmos. Ocean. Tech.*, **15**. 809-817.

Kummerow, C. D., D. –B. Shin, Y. Hong, W. S. Olson, S. Yang, R. F. Adler, J. McCollum, R. Ferraro, G. Petty and T. T. Wilheit, 2001: The evolution of the Goddard Profiling Algorithm (GPROF) for rainfall estimation from passive microwave sensors. *J. Appl. Meteor.*, **40**, 1801-1820.

Meneghini, R., and T. Kozu, 1990: *Spaceborne Weather Radar*. Artech House, 199 pp.

Nespor, V. and B. Sevruk, 1999: Estimation of wind-induced error of rainfall gauge measurements using a numerical simulation. *J. Atmos. Oceanic Technol.*, **16**, 450-464.

Nystuen, J. A., 1999: Relative performance of automatic rain gauges under different rainfall conditions. *J. Atmos. Oceanic Technol.*, **16**, 1025-1043.

Olson, W. S., Y. Hong, C. D. Kummerow, and J. Turk, 2001: A texture-polarization method for estimating convective-stratiform precipitation area coverage from passive microwave radiometer data. *J. Appl. Meteor.*, **40**, 1577-1591.

Ott, R. L., and M. Longnecker, 2001: *An Introduction to Statistical Methods and Data Analysis*. Wadsworth Group, 1152 pp.

Petty, G. W., 1994: Physical retrievals of over-ocean rain rate from multichannel microwave imager. Part I: Theoretical characteristics of normalized polarization and scattering indices. *Meteor. Atmos. Phys.*, **54**, 79-99.

Roberti, L., J. Haferman, and C. Kummerow, 1994: Microwave radiative transfer through horizontally inhomogeneous precipitating clouds. *J. Geophys. Res.*, **99**, 16707-16718.

Rudolf, B., H. Hauschild, W. Ruth, and U. Schneider, 1996: Comparison of raingauge analyses, satellite-based precipitation estimates, and forecast model results. *Adv. Space Res.*, **18**, 53-62.

Serra, Y. L., P. A'Hearn, H. P. Freitag, and M. J. McPhaden, 2001: ATLAS self-siphoning rain gauge error estimates. *J. Atmos. Ocean. Tech.*, **18**, 1989-2002.

Serra, Y. L. and M. J. McPhaden, 2002: Multiple Time and Space Scale Comparisons of ATLAS Buoy Rain Gauge Measurements to TRMM Satellite Precipitation Measurements. Submitted to *J. Appl. Meteor.*

Thiele, O. W., M. J. McPhaden, and D. A. Short, 1995: Optical rain gauge performance. *Proc. of the Second Workshop on Optical Rain Gauge Measurements*, Greenbelt, MD, NASA, 76 pp.

Viltard, N., C. Kummerow, W. S. Olson, and Y. Hong, 2000: Combined use of the radar and radiometer of TRMM to estimate the influence of drop size distribution on rain retrievals. *J. Appl. Meteor.*, **39**, 2103-2114.

Wilheit, T. T., A. Chang, and L. Chiu, 1991: Retrieval of monthly rainfall indices from microwave radiometric measurements using probability density function. *J. Atmos. Oceanic Technol.*, **8**, 118-136.

COMPARING TRMM RAINFALL RETRIEVAL WITH NOAA BUOY RAIN GAUGE DATA

A Thesis

by

AMY BLACKMORE PHILLIPS

Submitted to the Office of Graduate Studies of
Texas A&M University
in partial fulfillment of the requirements for the degree of

MASTER OF SCIENCE

December 2002

Major Subject: Atmospheric Sciences

ABSTRACT

Comparing TRMM Rainfall Retrieval

with NOAA Buoy Rain Gauge Data. (December 2002)

Amy Blackmore Phillips, B.S., University of Missouri

Chair of Advisory Committee: Dr. Gerald North

This study compares rain rate measurements from the Tropical Rainfall Measuring Mission (TRMM) satellite to rain rate measurements from rain gauges on open-ocean buoys. The rain gauges are part of the instrument package on the Next Generation Autonomous Temperature Line Acquisition System (ATLAS) buoys in the Tropical Atmosphere-Ocean/Triangle Trans-Ocean Buoy Network (TAO/TRITON) array in the tropical Pacific. The rain rate data from TRMM and 25 buoys are collected from January of 1998 to December of 2001. TRMM's 3G68 product provides instantaneous rain rate data averaged over 0.5° x 0.5° latitude-longitude grid boxes for the TRMM Microwave Imager (TMI), Precipitation Radar (PR), and a combined algorithm (COMB). The buoy's rain rate data are averaged over and reported in 10-minute intervals. Buoy data are compared to 1.0° x 1.0° TRMM area-averaged values centered on each of the 25 buoy locations. The 1.0° x 1.0° boxes are composed of four 0.5° x 0.5° 3G68 grid boxes.

The OVERLAP subset consists of all TRMM (TMI, PR and COMB) and buoy rain rate data from the observation period of January 1998 to December 2001. The MATCH dataset consists of only those 10-minute periods where both TRMM and the buoy data

are available. The rain rates from both subsets are averaged and compared to each other. Scatterplots are drawn, the best-fit line is determined, and the 95% confidence interval on the slope of the best-fit line is calculated. If the confidence interval contains 1.0, the two methods of measuring rain rates are not biased. This study shows that the confidence intervals for the OVERLAP and MATCH TMI versus buoy cases do contain 1.0. The confidence intervals for the OVERLAP and MATCH PR versus buoy and COMB versus buoy cases, however, do not.

This study concludes that TMI and the buoy rain rate measurements are unbiased and that the PR and COMB product underestimate rain rate as compared to the buoy.

ACKNOWLEDGMENTS

I would like to thank my committee chair, Dr. North, and my committee members Dr. Bowman and Dr. DiMarco for all of their advice and support throughout the course of this study. I am grateful to the United States Air Force for allowing me this unique opportunity to obtain my degree. All of the faculty and students have been an incredible help to me.

I would like to extend my sincere gratitude to my husband, Steve. He has been a tremendous motivating force during my time at A&M.

TABLE OF CONTENTS

	Page
ABSTRACT	iii
ACKNOWLEDGMENTS	v
TABLE OF CONTENTS	vi
LIST OF FIGURES	viii
LIST OF TABLES	ix
CHAPTER	
I INTRODUCTION	1
II BACKGROUND	5
2.1 Microwave Radiative Transfer	5
2.2 Spaceborne Weather Radar	7
III RAIN GAUGE, TMI, AND PR	8
3.1 Rain Gauge Measurements	8
3.2 TMI Instrument	9
3.3 TMI Algorithm	10
3.4 PR Instrument	13
3.5 PR Algorithm	13
3.6 COMB Algorithm	16
IV PREVIOUS WORK	17
4.1 Rain Gauge	17
4.2 TMI	20
4.3 PR	21
4.4 TMI and PR	22

CHAPTER Page

V DATA AND METHODS 23

5.1 Buoy Data 23
5.2 Buoy Data Quality Control 25
5.3 3G68 Data 27
5.4 Comparison Methods 28
5.5 Statistical Methods 29

VI RESULTS 34

6.1 OVERLAP Subset 34
6.2 MATCH Subset 34

VII SUMMARY AND CONCLUSIONS 39

REFERENCES 41

APPENDIX A 43

APPENDIX B 45

VITA 47

LIST OF FIGURES

FIGURE		Page
1	Locations of Next Generation ATLAS buoy used in the study.....	24
2	Length of OVERLAP time periods for January-December 1998-2001 for TRMM and buoys.....	30
3	Scatterplots of OVERLAP (a) TMI mean rainfall rate (mm hr^{-1}; ordinate) vs. buoy mean rainfall rate (mm hr^{-1}; abscissa); (b) as in (a), but PR mean rainfall rate vs. buoy mean rainfall rate; (c) as in (a), but COMB mean rainfall rate vs. buoy mean rainfall rate	36
4	Same as in FIG. 3, but for the MATCH subset	37

LIST OF TABLES

TABLE		Page
1	Number of OVERLAP and MATCH observations	31
2	Statistics information for the OVERLAP and MATCH subsets	38
3	Mean rain rate data (mm hr^{-1}) plotted in FIG. 3.	45
4	Mean rain rate data (mm hr^{-1}) plotted in FIG. 4.	46

CHAPTER I

INTRODUCTION

The region of the earth between 30°N and 30°S is defined as the Tropics. Seventy-five percent of the earth's surface area in the Tropics is ocean and two-thirds of the world's precipitation falls in the Tropics. Because the atmosphere receives three-fourths of its heat energy from latent heat released by precipitation, half of the earth's overall heat energy is due to tropical precipitation (Kummerow et al. 1998*)*. Large scale dynamics dictate that these energy releases associated with tropical precipitation events affect the entire global circulation pattern.

It is important to be able to quantify the amount of precipitation that falls in a given area so that climate modelers understand where and how much heat is released into the atmosphere from tropical precipitation events. There are several observing systems that are used to measure rainfall, such as *in situ* rain gauges, satellite systems, and weather radars (Nystuen 1999*)*.

Rain gauges are deployed on some deep ocean buoys, including the Next Generation Autonomous Temperature Line Acquisition System (ATLAS) buoys that comprise most of the Tropical Atmosphere-Ocean/TriangleTrans-Ocean Buoy Network (TAO/TRITON) array in the tropical Pacific Ocean. This array consists of approximately 70 Next Generation ATLAS and TRITON buoys between 8°S and 8°N,

---

This thesis follows the style and format of the *Journal of Climate*.

137°E to 95°W. The gauges used are RM Young Model 50203-34 capacitance-type rain gauges. There are 28 Next Generation ATLAS moorings in the TAO/TRITON array that have the RM Young capacitance rain gauges. The Pacific Marine Environmental Laboratory (PMEL) of the National Oceanic and Atmospheric Administration (NOAA) is responsible for the development and maintenance of the buoys. Data from this buoy program have widespread application in research related to climate variability and ocean-atmosphere interaction (Serra et al. 2001).

Moorings were deployed as part of the array beginning in November of 1984 and the TAO buoy array was completed in December of 1994. At that time, the TAO array utilized Standard ATLAS moorings. The Next Generation ATLAS moorings were later developed primarily to improve upon the Standard ATLAS moorings by upgrading data quality, reducing cost, and adding new sensors, such as the rainfall sensor. The first Next Generation ATLAS mooring was deployed in May of 1996. In November of 2001, Next Generation ATLAS moorings replaced all Standard ATLAS moorings (http://www.pmel.noaa.gov/tao/proj_over/mooring.shtml).

Next Generation ATLAS moorings can be deployed in water depths ranging from 1500 to 6000 m. Non-rotating wire rope is used from the surface to 700 m as a guard against fish bites. Plaited nylon line is used for the remainder of the mooring. The anchors weigh from 1900 to 2000 kg and are made from scrap railroad wheels. The buoy itself weighs 660 kg and has a net buoyancy of 2300 kg. It is a 2.3 m diameter fiberglass-over-foam toroid that has an aluminum tower as well as a stainless steel bridle (http://www.pmel.noaa.gov/tao/proj_over/mooring.shtml).

In addition to rain gauges, satellites are another platform used to measure rainfall. Visible, infrared (IR), and microwave imagery have been used to provide estimates of rainfall. Visible and IR sensors only have the ability to measure cloud top temperature and other similar physical properties. Microwave radiation, on the other hand, interacts directly with the precipitating hydrometeors. It is in this sense that microwave measurements of rainfall are more physically based than either visible or IR measurements.

The first microwave radiometer, the Electrically Scanning Microwave Radiometer (ESMR), was launched in 1972 as part of the payload on the Nimbus-5 satellite to make global rainfall measurements. Since then, there have been many other missions that involve the microwave measurement of rainfall. The most recent mission, the Tropical Rainfall Measuring Mission (TRMM), was launched in November of 1997 as a collaborative effort between the National Aeronautics and Space Administration (NASA) of the United States and the National Space Development Agency (NASDA) of Japan. The objective of TRMM is to measure rainfall and energy (i.e., latent heat of condensation) release of tropical and subtropical regions of the world (Kummerow et al. 1998).

The TRMM satellite is in a circular orbit 350 km above the earth and is oriented at a 35° inclination angle with respect to the equatorial plane. TRMM has three instruments that measure rainfall: the TRMM Microwave Imager (TMI), the Precipitation Radar (PR), and the Visible and Infrared Radiometer System (VIRS). This study focuses on rain rate measurements derived from TMI and PR separately, as well as

values derived from a combined algorithm (referred to COMB) which utilizes information from both the TMI and PR.

The launch of TRMM marked the first time a space-based radar was deployed to measure precipitation. The PR provides a three-dimensional space-based view of precipitation over the tropics. Traditional ground-based weather radars can also be used to measure tropical rainfall since many are located in coastal regions.

CHAPTER II

BACKGROUND

2.1 Microwave Radiative Transfer

The radiance of an object is defined as the rate of emission of photons per unit area per unit solid angle. The radiance of a blackbody, B_λ, is described by the Planck function:

$$B_\lambda(T) = \frac{2hc}{\lambda^5} \cdot \frac{1}{\exp(hc / \lambda kT) - 1} , \qquad (1)$$

where λ is wavelength, T is temperature, h is Planck's constant , k is Boltzmann's constant, and c is the velocity of light. For microwave wavelengths (1 mm $\leq \lambda \leq$300 mm) and typical temperatures of the Earth (T $\geq$ 200 K), the radiance is approximately linearly proportional to the temperature. This is called the Rayleigh-Jeans approximation, where a brightness temperature is defined as the emission of a pure blackbody that is defined by a single temperature.

The microwave radiances observed by a spaceborne radiometer are influenced by surface characteristics (i.e., land versus water), atmospheric constituents affecting absorptivity, and large precipitation drops that scatter microwave radiation. Since this study involves microwave measurements over the Pacific Ocean, it is important to consider ocean surface characteristics. The emissivity of the ocean's surface depends on temperature, salinity, and surface roughness. Overall, in the microwave region, the ocean's emissivity is rather low; 0.4 to 0.5 at nadir. This means that oceans appear cold relative to its surroundings in microwave images.

There are three important atmospheric absorbers and emitters of microwave radiation: molecular oxygen, water vapor, and liquid water drops. Molecular oxygen exhibits many absorption lines near 60 GHz as well as another absorption line at 118 GHz. Water vapor exhibits an absorption line at 22.235 GHz and at 183 GHz. The third important atmospheric absorber, liquid water drops, can be categorized as non-precipitating cloud liquid water (NCLW) and rain. Since NCLW drops are smaller than the wavelengths of microwave radiation, the Rayleigh approximation may be used. Rain drops, however, have diameters comparable to microwave wavelengths. Because of this, scattering becomes important and Mie theory can be used to calculate scattering properties if the drops are assumed to be spherical (Kummerow et al. 2001), which is a widely accepted assumption.

There are two different types of passive microwave measurements of rainfall: scattering and emission. Scattering-based methods depend on the strong scattering of ice in upper portions of precipitation regions. Emission-based methods depend on the absorption and emission of liquid phase cloud droplets and rain drops. Scattering is applicable at frequencies greater than 60 GHz over both land and ocean backgrounds. Below 22 GHz and over an ocean background, emission is valid because emission-based methods require a radiometrically cold background such as the ocean. Rain has a high emissivity (emissivity = 0.9) and appears warm in microwave images. Thus, rain falling over the ocean is easily detected because it appears warm against a cold ocean background.

2.2 Spaceborne Weather Radar

The radar equation describes the average power, $\overline{P}$, returned from a sample volume:

$$\overline{P} = \frac{P_T \, G^2 \, \lambda^2 \, \theta \, \phi \, h}{512 \, \pi^2 \, r^2 \, \ln 2} \sum_{vol} \sigma_{bsi} \, . \tag{2}$$

In the above equation, P_T is the transmitted power, G is the gain, λ is the wavelength, θ is horizontal beamwidth, ϕ is vertical beamwidth, h is pulsewidth, r is range, and σ_{bsi} is the backscattering cross section of a single hydrometeor. The variables in the numerator are related to radar hardware. The backscattering cross section and the range are target characteristics.

Unlike the radiometer, radar has the ability to sample storms vertically. In addition, radar is unaffected by land's high emissivity. These advantages were recognized as early as the 1950's (Meneghini and Kozu 1990), but due to cost, weight, power, and reliability issues inherent to space-based radar systems, radar was not used in space until TRMM was launched in 1997. The limited temporal sampling of a space-based radar is insufficient to characterize rain over areas on the order of 100 km^2 on a daily basis. Repeated sampling over many days, however, makes it possible to estimate time-averaged rain rates (Meneghini and Kozu 1990).

CHAPTER III

RAIN GAUGE, TMI, AND PR

3.1 Rain Gauge Measurements

Prior to the use of RM Young rain gauges, mini-optical rain gauges were used on TAO buoys in the Pacific warm pool during the Tropical Ocean Global Atmosphere Coupled Ocean Atmosphere Response Experiment (TOGA COARE). Thiele et al. (1995) indicate that the mini-optical gauges err on the order of 15 to 20%. Unlike the mini-optical gauges, the RM Young self-siphoning rain gauge can be calibrated before and after deployment. The transition from mini-optical rain gauges to the RM Young gauges occurred from 1995 to 1998 (Serra et al. 2001).

The rain rate data used in this study are collected in the RM Young Model 50203-34 rain gauge which is positioned 3.5 m above the ocean surface and has a maximum capacity of 500 ml. Once maximum capacity is reached, the gauge empties. This self-siphoning process takes place over a 30-second period. A stainless steel rod covered by a teflon sheath sits inside the cylindrical collection chamber and acts as a probe. The water acts as the outer plate of a capacitor and the metal rod acts as the inner plate. As the water height in the collection chamber increases, the surface area of the capacitor increases thus increasing the capacitance. The capacitance is measured and converted to water height in the collection chamber. The capacitance is translated to frequency. The frequency is then averaged over one-minute intervals, and output digitally in counts. To convert to water volume, the equation,

$$V = \frac{a}{N} + b, \qquad (3)$$

is used, where V is the volume of water in ml, N is the counts, a is in ml-counts, and b is given in ml. Both a and b are calibration coefficients found through least-squares regression of V on N^{-1}. To convert volume to accumulations, the siphon events must be removed from the data set. During post-deployment processing of the data, three minutes of data centered on the siphon event are removed.

The buoys continuously collect rain data, but only store the one-minute volume samples on board while deployed at sea. The daily mean and standard deviation of rain rate and the daily percent time raining, which are calculated from the one-minute volume data, are sent to PMEL via Service Argos, Inc. Service Argos, Inc. uses NOAA polar orbiting weather satellites for data telemetry. Once the data are recovered, the 1-minute accumulations are filtered with a 16-minute Hanning filter to generate smoothed 10-minute accumulations. The 10-minute rain rates are then calculated by differencing the 10-minute accumulation data and then converting to mm hr^{-1}.

3.2 TMI Instrument

The TMI is a nine-channel passive microwave radiometer that is based almost entirely upon the Special Sensor Microwave/Imager (SSM/I) which was flown on board the Defense Meteorological Satellite Program (DMSP) satellites. The main differences between TMI and SSM/I are the addition of a pair of 10.7 GHz channels with both horizontal and vertical polarizations and a shift of the water vapor frequency channel from 22.235 to 21.3 GHz. This shift is done to avoid the saturation of this channel in the

tropics. TRMM also has a higher spatial resolution than the SSM/I due to its lower orbit (Kummerow et al. 1998).

The TMI antenna is an offset parabola with a 61 cm aperture and a focal length of 50.8 cm. The antenna beam views the earth's surface at an angle of 49° from nadir, resulting in a 52.8° incidence angle at the earth's surface. The data from the TMI come from the forward 130° of the circle it traces on the earth's surface. The 130° used for data acquisition yields a swath width of 758.5 km.

3.3 TMI Algorithm

There are two rainfall retrieval algorithms that are utilized by TMI. One of the algorithms is based on the use of emission signatures of the 19.3- and 21.3-GHz channels described in Chang et al. (1993) and Wilheit et al. (1991). These distinct signatures are used to retrieve rainfall over the ocean since the ocean surface appears radiometrically cold to a microwave sensor. The other algorithm is the Goddard Profiling Algorithm (GPROF). GPROF is designed to retrieve the instantaneous rain as well as the vertical structure of rain.

GPROF was first detailed in Kummerow et al. (1996). The motivation behind developing GPROF was the TRMM mission. There were two important requirements for GPROF. One requirement was for it to have simple computations so that it would process swiftly. The other requirement was for individual processes within the retrieval to be distinct and identifiable so that their effect upon the final result would be known.

The overall basis of the algorithm is the Bayesian approach (described later in this section).

The Goddard Cumulus Ensemble (GCE) is used to produce probability density functions of rain profiles. Radiative transfer calculations determine the GCE's upwelling brightness temperatures which serve to establish the similarity of radiative signatures, ultimately providing the probability that an actual profile is observed. In this study I use GPROF version 5, which has four main improvements to earlier versions. The three improvements related to this study are the following: 1) implementation of a more accurate representation of the freezing level (Wilheit et al. 1991); 2) utilization of new convective-stratiform separation techniques; 3) inclusion of emission and scattering indices and the National Environmental Satellite, Data, and Information Service (NESDIS) operational rainfall relationship over land.

Studies using radar to determine the freezing level have shown the resulting freezing level to be higher than the climatological freezing level data (Kummerow et al. 2001). Use of the climatological freezing level data would give erroneously low freezing levels, which in turn gives an overestimation of rainfall in the middle and high latitudes. In Wilheit et al. (1991), the 19- and 22-GHz channels are used to estimate freezing levels. These freezing levels represent the rain layer thickness and the atmospheric water vapor content in the radiative transfer model. The updated convective-stratiform separation techniques are detailed in Olson et al. (2001). Emission and scattering index information are detailed in Petty (1994).

In the Bayesian inversion approach, each channel has to be weighted by the uncertainty in that channel. This uncertainty is the sum of the uncertainty in the measurement and in the forward model. The version 4 GPROF assigned an equal weight to all of the channels, while the version 5 GPROF incorporates polarization-based emission and scattering indices. This has two advantages: 1) these indices isolate the signal coming from the rain cloud itself from the background variability and 2) they are monotonic functions of the rainfall emission or ice scattering intensity. They also distinguish the effects of scattering from emission-attenuation effects, so that frozen hydrometeors can be distinguished from liquid precipitation and cloud.

GPROF has some weaknesses that are currently being addressed. First, upgraded cloud resolving models need to be included in the *a priori* database since new discoveries about the treatment of ice microphysics have been made. Since retrieving rainfall is a three-dimensional issue, a three-dimensional Monte Carlo radiative transfer calculation will be used in future versions of GPROF instead of the current one-dimensional Eddington approximation (Kummerow 1993). In the Monte Carlo calculation, the photons are traced backward from the point where the brightness temperature is computed to where it is absorbed. It is considered to be emitted at this absorption point with the brightness temperature equaling the medium's physical temperature (Roberti et al. 1994). Inclusion of the different cloud resolving models and different radiative transfer calculation will give explicit treatment of the melting layer.

In addition consistency between GPROF's physical assumptions and the assumptions in the PR algorithm (Viltard et al. 2000). Smaller drops are used in the PR

algorithm. There are also different classifications of stratiform versus convective rainfall in the two algorithms, plus there is no melting level in GPROF. Data dealing with these three issues are currently being analyzed. Another issue that is being investigated is the incorporation of realistic simulations of extratropical weather into GPROF.

3.4 PR Instrument

Unlike the TMI, the PR is an active microwave sensor. It is a system that operates at 13.8 GHz (2.17 cm wavelength) as a 128 element active phased array (Kummerow 1998). The PR's pulselength is 1.6 microseconds. The pulses are transmitted at a fixed pulse repetition frequency of 2776 Hz giving 64 independent samples. It has an effective signal-to-noise ratio of around 4 dB for a 0.7 mm hr^{-1} rain rate. When the PR is in observation mode it scans in the cross-track direction over +/- 17°, which is equivalent to a 215 km swath width.

3.5 PR Algorithm

The PR algorithm, or 2A25 algorithm, has been generating the version 5 products since November of 1999. Data files named 1C21, 2A21, and 2A23 are input into the 2A25 algorithm. The 1C21 provides the measured vertical profiles of reflectivity factor, Z_m's , the 2A21 provides an estimate of path attenuation and 2A23 provides rain type, brightband height and freezing level information. Once these data files have been input, the 2A25 algorithm estimates the true effective reflectivity factor, Z_e, at 13.8 GHz at each radar resolution cell from the Z_m.

The 2A25 first defines the region for processing and selects the range gates between the rain top and the lowest height above the surface that is free from clutter. The brightband height and the climatological surface atmospheric temperature define the different phase states of the precipitation. Initial values of the coefficients in the k-Z_e and Z_e-R relationships at different altitudes are defined accordingly. The k is the specific attenuation and the R represents rain rate.

The attenuation correction is based upon a hybrid of the surface reference method and the Hitschfeld-Bordan method (Iguchi and Meneghini 1994). The surface reference method estimates the path-integrated attenuation (PIA), which is the attenuation to the surface, through rain from the decrease in surface return. When the wavelength used is small, the signal is attenuated. Hitschfeld and Bordan derived a power-law relation between Z and k so that they can be solved for a given function Z_m. The relationship is:

$$k = \alpha Z_e^{\beta}. \qquad (4)$$

The α and β both represent attenuation by intervening cloud, atmospheric gases and precipitation (Hitschfeld and Bordan 1954). This solution gives a reasonable estimate if the attenuation effect is small. The coefficient α in the k-Z_e relationship is adjusted so that the PIA estimated from the measured Z_m profile by the Hitschfeld-Bordan method matches the estimate of PIA from the surface reference method. Attenuation-corrected Z_e at all ranges are calculated by using the Hitschfeld-Bordan method with the modified α. The α-adjustment method assumes that the differences between the PIA estimate from the surface reference and that from the measured Z_m profile result from a bad

choice of α due to the differences between the assumed and actual drop-size distribution (DSD). It also assumes that the radar is properly calibrated and that Z_m is unbiased (Iguchi et al. 2000).

Rain rate is calculated from Z_e using

$$R = a\, Z_e^{\,b}. \qquad (5)$$

The variables a and b are functions of the rain type and height of the 0° isotherm and storm top (Iguchi et al. 2000). Rain type, bright band, phase state, temperature and differences in terminal velocity are taken into account. The initial values of a and b are modified according to the adjustment in α so that the k-Z_e and Z_e-R relationships are consistent with one of the two assumed DSD models. One is given for convective precipitation and another is given for stratiform precipitation. The coefficient a is further modified by the index of nonuniformity. The nonunifrom beamfilling effect of rain on the Z_e-R relation is typically less than 5%. In this algorithm, the maximum correction is limited to 20%.

It is important to know the appropriate k-Z_e and Z_e-R relations in order for an algorithm to estimate rain rate without bias. This is made easier because PR is a space-based radar, and as a result, the surface reference method can be used. The surface reference method allows a narrowing of the DSD. Nonuniform rain distribution within the radar resolution cell may become a large error source when the attenuation is severe. The algorithm uses a first-order correction to mitigate this problem. The validity of this nonuniform beamfilling correction method is yet to be verified.

3.6 COMB Algorithm

The COMB algorithm takes information from the TMI and from the PR. The concept behind the algorithm is simple; to utilize the combined strengths of the individual instruments. Since PR has a higher resolution than TMI the PR can compensate for the TMI in this respect. The TMI can compensate for errors the PR can make when estimating integrated quantities. The algorithm is based upon the rain profile as indicated by PR's reflectivities while checking consistency with TMI's estimate of total attenuation. For data comparisons between the two instruments to be made, both data sets are expressed in terms of DSD variables. A Bayesian approach is used to condition the *a priori* probability density function of the DSD variables to the PR and TMI measurements (Haddad et al. 1997).

CHAPTER IV

PREVIOUS WORK

4.1 Rain Gauge

The first systematic evaluation of the RM Young rain gauge on board the ATLAS buoys was carried out by Serra et al. (2001). Errors in rain rate were determined by analyzing data from rain gauges as well as through laboratory experiments. In that case study, noise is seen as the small fluctuation of rain rate about the zero mark. The smallest noise amplitudes were seen during the dry periods. Negative rain rates in the data set were generated by random noise. Rain gauge observations indicate that negative rain rates occur more frequently during times of significant rainfall. Observations also indicate that random noise can occur during times of less rainfall, or dry periods. Dry periods are defined as 20-minute periods with no more than one value between 0.5 and 3.0 mm hr^{-1} for the 10-minute data. It was hypothesized that the observed noise and its dependence on volume could be related to the circuit design of the rain gauges. From equation 3, it is implied that tube volume resolution is inversely related to counts. Decreases in resolution with increasing volume means greater errors in the recorded volumes. Because of this, there will be greater errors in the rain rates (Serra et al. 2001).

The volume measurements were also discovered to be sensitive to the diurnal temperature cycle with larger volumes seen for cooler nighttime temperatures, around sunrise. The situation was reversed at sunset. The differences between daytime and nighttime volume measurements led to differences in rain rate on the order of hundredths

of millimeters per hour (Serra et al. 2001). The effect of temperature on volume measurements could have been responsible for volume measurements reading high during rain events. The measurements stabilized to lower values soon after the rain events were over. It was hypothesized that the circuitry was sensitive to temperature, and since the circuitry is close to the fill tube this would explain why the volume read higher during rain events. If it is assumed that the rain is colder than the ambient air, the volume will increase just like in the sunrise situation. Decreases in accumulation during the stabilization time can be seen as negative rain rates in the 10-minute data if the stabilization times are longer than 10 minutes (Serra et al. 2001).

To determine the behavior of the rain gauge during periods of significant rain, lab experiments were carried out. A constant known flow rate was applied to a rain gauge with a mechanical pump accurate to 1%. The results indicate that higher noise levels were prevalent around siphon events. This noise was primarily the result of nonlinear behavior assumed in the conversion from counts to volumes in equation 3. Because siphon events take a short period of time, only 30 seconds, error estimates for periods of active accumulation assume these errors are negligible. Overall, noise was larger in magnitude during rainy periods; approximately 0.4 mm hr^{-1} (Serra et al. 2001).

The evaporation rate was also estimated from the data. Evaporation was not thought to be a problem since the gauge is protected from the wind and sun. Loss of volume due to evaporation was found to be equivalent to about 6 mm in a month. Sometimes, a slow increase in accumulation was evident even when there was no rain present. This phenomena might be due to either sea spray or electronic drift of some

sensors. To estimate possible sea spray contamination, time periods with relatively high winds and no rain were analyzed. Results showed no obvious sea spray contamination (Serra et al. 2001).

Few studies have been done to quantify the error induced by wind on rain gauge collection efficiency. Most of them have dealt with rain gauges on board ships. Nespor and Sevruk (1999) modeled gauge efficiency by looking at how the prescence of a cylinder, which creates turbulent flow, affects the volume of drops passing a catchment surface area. They found that errors increase with increasing wind speeds, with decreasing drop sizes, and with decreasing rain rates. Therefore, light rain events are thought to cause more errors due to the wind. Based on this study, it was determined that undercatch of rain is expected to be on the order of 10-50% for these rain gauges. In the future, there will be a plan to develop a correction specific to these gauges.

Another recent study was done to compare TRMM satellite rainfall measurements to buoy rainfall measurements on several different time and space scales (Y.L. Serra, 2001, personal communication). This study looked at rain rates measured across 0.1°, 0.2°, 0.5°, 1.0°, 2.5° and 5.0° boxes on daily, monthly and seasonal time scales. Results indicate that TMI shows the best agreement in percent time raining with the buoys for 0.1° boxes on a daily time scale, while the PR shows large normalized biases in percent time raining for all areas for the same time scale. On monthly and seasonal time scales, the study indicates that TMI and PR both underestimate heavy rain events. When considering rain rate, the PR shows good agreement with the buoys on all time scales for the 0.5° boxes. TMI's rain rate agrees best with the buoys' for 1.0° boxes

on daily time scales and with the 0.1° to 0.5° boxes on monthly and seasonal time scales. On daily and monthly time scales, TMI gives greater maximum rain rates than the buoys. The PR shows greater maximum rain rates than the buoys on a monthly time scale. Overall, TMI and PR measured less total rainfall than the buoys during this study.

Serra and McPhaden (2002, manuscript submitted to *J. Appl. Meteor.*) looked at measurements of rainfall from TMI, PR, and 14 buoys in heavy rain areas of the tropical Pacific and Atlantic. They gathered rainfall information for the daily, monthly, and seasonal time scales and over spatial scales ranging from 0.1° to 5.0° squares centered on the buoys over a three year period. The results show that both TMI and PR both tend to underestimate rain rates as compared to the buoys. This underestimation is found to be greatest in the northeast Pacific and the Atlantic. For all time scales, the TMI rain rate agrees the best with the buoy rain rate on the 5.0° spatial scale.

4.2 TMI

There have been some studies that have been done to validate the GPROF algorithm, but they have mostly been done over land. Kummerow et al. (2001) looked at 20 to 40 rain gauges located on atolls in the Pacific Ocean. The atoll area was divided up into 2.5° grid boxes, and only three to four boxes had more than one gauge per box. Overall, GPROF was seen to underestimate precipitation by 9% when all of the atoll rain gauges were used. The rainfall correlation was 0.85 for this scenario. When grid boxes with more than one gauge were used, GPROF overestimated precipitation by 6%. The rainfall correlation value, 0.91, was high in this scenario.

The Global Precipitation Climatology Centre (GPCC) also did a study involving rain gauges (Rudolf et al. 1996). They took data from 6700 rain gauges and interpolated it into 0.5° latitude-longitude grid boxes. The data was then averaged over 2.5° grid boxes. It was shown that GPROF overestimates precipitation by 17% when compared to the rain gauge product. There was a correlation of 0.8 between the two products (Rudolf et al. 1996).

Kummerow et al. (2001) compared output from the GPROF algorithm with a ground-based radar located in Kwajalein. The GPROF can distinguish between land, which includes coastline, and ocean. This study only considered rainfall accumulations made over the ocean. The GPROF underestimated rainfall by 32% when compared to the ground-based radar. The correlation between the two products was 0.95.

4.3 PR

Comparisons of dBZ distributions between the PR and a WSR-88D radar in Melbourne, Florida, were made at 3 km above sea level. PR's data was corrected for attenuation using the hybrid approach described in Iguchi et al. (2000). The resulting histograms have a very similar distribution. Due to their different effective radar reflectivity factor, the PR shows consistently higher dBZ values than the WSR-88D. It is estimated that the difference in effective radar reflectivity factor becomes significant at 30 dBZ and increases to 2 to 3 dB in the 40 to 50 dBZ range (Iguchi et al. 2000). This study demonstrated the utility of Iguchi's hybrid approach.

4.4 TMI and PR

Viltard et al. (2000) used reflectivity output from the PR to create three-dimensional profiles of rain to put into a radiative transfer calculation and produce simulated brightness temperatures. These simulated brightness temperatures were then compared to the actual brightness temperatures as retrieved by the TMI. This allows the two instruments' output to be compared. It also allows for the determination of an appropriate DSD that would give consistent results between the two instruments. The results of this method yielded brightness temperature differences of 8 to 10 K, which is an error of less than 5%. It is interesting to note that the brightness temperature differences were not consistent across all of the channels.

Kummerow et al. (2001) compare the output of the GPROF algorithm and the PR algorithm's output and found that rain rate histograms for individual pixels are very similar in shape. Moreover, when rain rates are averaged over 0.5° grids, the resulting histograms from GPROF and PR were almost identical. An additional study analyzed the vertical structure of rain as derived from TMI and PR. TMI overestimates rain by approximately 42 mm at 3 to 4 km above the surface. The correlation coefficient between TMI and PR below 4 km is 0.91 above the ocean.

CHAPTER V

DATA AND METHODS

5.1 Buoy Data

One of the main data sources in this study is the TAO buoy rain gauge measurements. This data is available via the internet on PMEL's website (http://www.pmel.noaa.gov/tao/data_deliv/). Rain rates are averaged over 10-minute intervals. The report time of the buoy measurement is the midpoint of the 10-minute measuring interval. Shortly after TRMM's launch, at the beginning of 1998, the Next Generation ATLAS buoys had not fully replaced the Standard ATLAS buoys in the TAO array. Since Standard ATLAS buoys did not have the capability to measure rainfall, data for this study is taken from 25 Next Generation ATLAS buoys in the Pacific Ocean during the period of January 1, 1998 to December 31, 2001. The locations of the buoys used in this study are shown in FIG. 1.

The buoy data is stored in netCDF files, one buoy per file. The files contained date and time information and rain rate (in mm hr^{-1}). The files also contain quality codes. A code of 0 indicates that data is missing. A data quality code of 1 indicates that pre/post-deployment calibrations agree. The default quality code, 2, indicates that pre-deployment calibrations were applied. This quality code is the default value for sensors that are currently deployed as well as for sensors that were not recovered or sensors that were not able to be calibrated upon recovery. The 3 and 4 quality codes indicate that pre/post-deployment calibrations differ, original data does not agree with

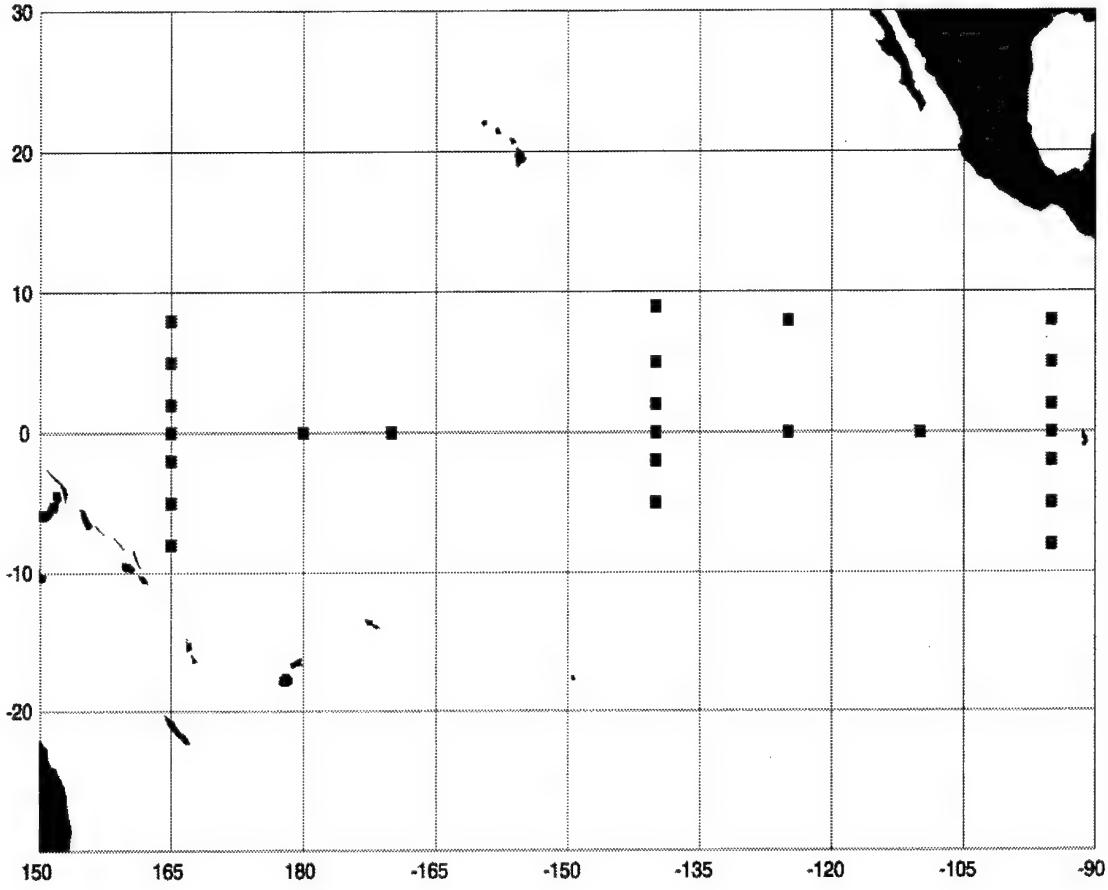

FIG. 1. Locations of Next Generation ATLAS buoys used in the study. Negative numbers indicate west longitude and south latitude.

other sources, or that the original data are noisy. When the code is 3, the data are adjusted to correct the error. In the case of code 4, the data could not be confidently adjusted to correct for the error. A code of 5 means that the sensor or tube failed. In this study, rain gauge data with quality codes of 1, 2 or 3 are used.

When the recovered sensor meets the nominal sensor drift criteria of 0.6 mm hr^{-1}, the quality code is changed from a 2 to a 1. When it does not meet this criteria, the quality code becomes 4. This code can later be changed to a 3 or 1 if an adjustment based on post-deployment calibrations is made. When the instrument is damaged or lost the quality code of 2 is assigned (http://www.pmel.noaa.gov/tao/proj_over/qc.html).

5.2 Buoy Data Quality Control

Real-time ATLAS data quality control is performed on a daily, weekly and monthly basis. Quality control on a daily basis first begins with flagging the data if they fall outside of the error specifications. Then the rest of the data are checked against more stringent requirements. The remaining data are flagged if they fall outside the smaller range of error specifications. If flagged, the data generate an error alert message. This alert signals a data analyst to determine if the flagged data are truly erroneous. Differences between TAO data processed at PMEL and the TAO data that are transmitted via the Global Telecommunications System (GTS) are investigated and corrected (http://www.pmel.noaa.gov/tao/proj_over/qc.html).

The mean daily rain rate and standard deviation are calculated every week at PMEL and are compared to Comprehensive Ocean-Atmosphere Data Set (COADS)

climatology. Error alerts occur when percent time raining is above 30% and when the rain rate is greater than 4.0 mm hr^{-1}. These alerts are investigated by an error analyst and the data are flagged if they are determined to be erroneous. The monthly quality control involves plotting the daily averaged rain rate by site for the past 12 months and is checked for continuity between deployments. These plots are also compared to COADS climatology.

Computer programs utilize pre-deployment calibrations to analyze raw data. These programs check for missing data as well as data that are physically impossible. A log of all potential data problems is generated from these programs. Time series plots, spectral plots and histograms are generated for all rainfall data. Basic statistics, such as the mean, median, standard deviation, variance, maximum and minimum are computed for each of the time series. These time series and statistics are analyzed by data analysts. Data that stand out in relation to its neighbors, or outliers, are examined closely. The mooring deployment and recovery logs are examined at the same time as the suspicious data to search for clues, such as a damaged sensor. When all checks have been made, if the data are still considered to be erroneous, they are flagged. A three-minute interval centered on siphon events is removed from the data set. Random spikes occurring during periods of rapid accumulation or surrounding siphon events are removed from the data set manually.

Rain rate calculations are sensitive to the noise in accumulations made over short time periods. To remedy this, the 1-minute accumulations are filtered with a 16-point Hanning filter and rates are then computed at 10-minute intervals. Residual noise in the

filtered time series includes false negative rain rates. These negative rain rates rarely exceed a few mm hr^{-1}, so they are not considered to be problematic (http://www.pmel.noaa.gov/tao/proj_over/qc.html).

After the rain gauge is recovered, post-deployment calibrations are made. The coefficients resulting from these calibrations are compared to the pre-deployment calibration coefficients. The calibration equation uses both the pre-deployment calibration coefficients and the post-deployment calibration coefficients separately along with a set of input values to generate pre- and post-deployment output values.

5.3 3G68 Data

The second source of data is the TRMM 3G68 gridded product. These data are available from TRMM Science Data and Information System, or TSDIS (http://tsdis.gsfc.nasa.gov/trmmopen/index.html). Unlike the buoy data, the 3G68 product is organized by day instead of by location. Data are provided in 0.5° x 0.5° latitude-longitude grid boxes, or cells. The observation time for each grid box is recorded to the nearest minute. More than one 3G68 observation may occur in a single grid box in one day. The data include retrievals from three different algorithms: the TMI, the PR, and the COMB. In addition to the mean rain rate for each algorithm, the data set includes the number of pixels TMI, PR and COMB observed, the number of rainy pixels observed by TMI, PR and COMB, and the percentage of rain that was convective. The 3G68 data span the entire four year period.

5.4 Comparison Methods

Because the TAO buoys are nominally located at longitudes and latitudes corresponding to the corners of the 3G68 grid boxes (rather than the centers), the buoy data are compared to TRMM area-averaged values for 1.0° x 1.0° boxes centered on each of the 25 buoy locations. The 1.0° x 1.0° boxes are composed of four 0.5° x 0.5° 3G68 grid boxes. Because the buoy rain rate data are averaged over and reported in 10-minute intervals, the 1.0° x 1.0° TRMM values are also organized into the same 10-minute intervals. This allows for matching buoy and TRMM rain rate data on spatial scales of 1.0° x 1.0° and a time scale of 10 minutes. TRMM measurements are typically available between zero and two times per day in each 1.0° x 1.0° box.

Statistics are presented below for two different subsets of the data. The first subset is the OVERLAP subset. For each buoy the overlap period extends from the first available day of buoy data to the last available day. During the overlap period for each buoy, there are missing data in both the TRMM and buoy records. This subset includes a large number of 10-minute observations between the approximately twice-daily TRMM fly-overs. FIG. 2 shows the length of the OVERLAP subsets for each buoy.

The second subset, the MATCH subset, consists of only those 10-minute periods where both TRMM and the buoy data are available, including 0.0 mm hr^{-1}. This method reduces the buoy data from nominally 144 10-minute measurements per day to between 0 and 2 10-minute observations per day . TABLE 1 shows the number of observations in each subset.

5.5 Statistical Methods

The mean and the variance are computed for all buoy and TRMM data in the OVERLAP and MATCH subsets. Scatterplots of buoy mean rain rate versus the respective TRMM instrument mean rain rate are plotted in Chapter 6 for each situation: OVERLAP and MATCH. A linear least-squares method is used to fit a line to the scatterplot data. This method determines the slope and intercept that minimizes the total squared prediction error. The prediction errors are the data's y-value deviations from this least-squares line, or regression line. In this experiment, the regression line is used to predict the y-values (TRMM rain rate values) from the x-values (buoy rain rate values), as the buoy measurements are taken to be ground truth. The estimate of slope is:

$$\hat{\beta}_1 = \frac{S_{xy}}{S_{xx}}, \tag{6}$$

where S_{xy} is the sum of x deviations times y deviations, given by:

$$S_{xy} = \sum_i (x_i - \bar{x})(y_i - \bar{y}), \tag{7}$$

and S_{xx} is the sum of x deviations squared,

$$S_{xx} = \sum_i (x_i - \bar{x})^2 \ . \tag{8}$$

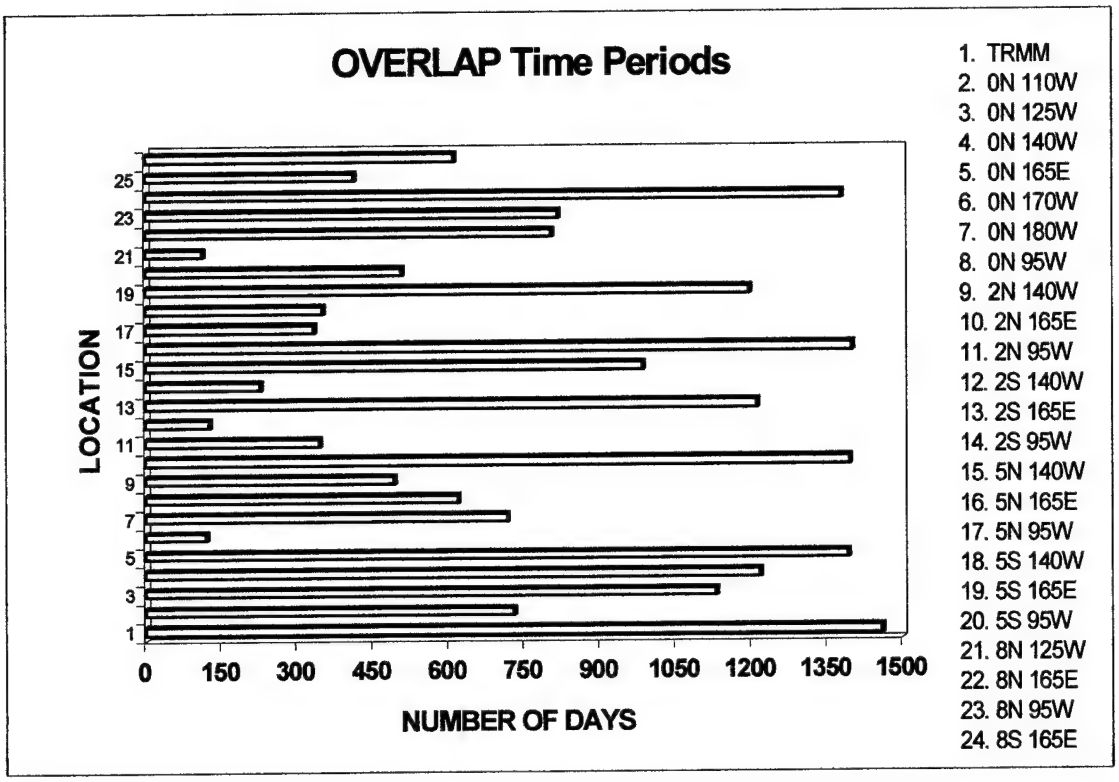

FIG. 2. Length of OVERLAP time periods for January-December 1998-2001 for TRMM and buoys.

TABLE 1. Number of OVERLAP and MATCH observations. The values in the # column refer to the legend values in FIG. 2.

			OVERLAP				MATCH		
#	**Lat**	**Long**	**Buoy**	**TMI**	**PR**	**COMB**	**TMI**	**PR**	**COMB**
2	**0° N**	**110° W**	100354	866	349	349	828	334	334
3	**0° N**	**125° W**	149490	1347	535	535	1236	491	491
4	**0° N**	**140° W**	154950	1456	575	575	1285	515	515
5	**0° N**	**165° E**	101456	1659	656	656	837	335	335
6	**0° N**	**170° W**	17276	138	55	55	138	55	55
7	**0° N**	**180° W**	78860	860	332	332	656	258	258
8	**0° N**	**95° W**	85860	731	291	291	703	281	281
9	**2° N**	**140° W**	70498	588	236	236	584	236	236
10	**2° N**	**165° E**	166657	1663	662	662	1374	557	557
11	**2° N**	**95° W**	49637	415	163	163	414	163	163
12	**2° S**	**140° W**	18139	151	61	61	151	61	61
13	**2° S**	**165° E**	78919	1457	575	575	653	254	254
14	**2° S**	**95° W**	22951	277	110	110	193	76	76
15	**5° N**	**140° W**	141359	1182	469	469	1178	467	467
16	**5° N**	**165° E**	158767	1694	662	662	1324	523	523
17	**5° N**	**95° W**	47973	413	161	161	412	160	160
18	**5° S**	**140° W**	50485	423	163	163	423	163	163
19	**5° S**	**165° E**	110102	1446	571	571	923	363	363
20	**5° S**	**95° W**	57775	614	242	242	483	191	191
21	**8° N**	**125° W**	16268	139	53	53	139	53	53
22	**8° N**	**165° E**	88323	978	381	381	743	294	294
23	**8° N**	**95° W**	44901	1007	405	405	388	154	154
24	**8° S**	**165° E**	186600	1682	656	656	1577	623	623
25	**8° S**	**95° W**	49429	424	168	168	421	167	167
26	**9° N**	**140° W**	87649	757	302	302	753	299	299

The estimate of the intercept is:

$$\hat{\beta}_0 = \bar{y} - \hat{\beta}_1 \bar{x} \qquad (9)$$

Since the regression line is a predicted line, there is some inherent uncertainty. This uncertainty is the sample mean squared prediction error and is represented by s_ε^2. In order to determine s_ε^2, the residuals are calculated. The residuals are simply the prediction errors in the sample and are given by the actual values minus the predicted values.

$$residuals = y_i - \hat{y}_i \qquad (10)$$

The sample mean squared prediction error is

$$s_\varepsilon^2 = \frac{\sum_i (y_i - \hat{y}_i)^2}{n - 2} \qquad (11)$$

where n is the number of data points in the sample. In this case, n equals 25 so the degrees of freedom are 23 assuming that the stations are independent of one another. The square root of s_ε^2 is called the standard error of estimate. It estimates the standard deviation of the sample y-values associated with the given x-values. About 95% of the prediction errors will fall within 2 standard deviations of the mean error (Ott and Longnecker 2001).

The confidence interval for both the slope and intercept is the estimate plus or minus the test statistic from a Student's t-distribution times the standard error. The confidence interval for the slope is given by:

$$\hat{\beta}_1 \pm t_{\alpha/2} s_\varepsilon \sqrt{\frac{1}{S_{xx}}} \qquad (12)$$

The confidence interval for the intercept is given by:

$$\hat{\beta}_0 \pm t_{\alpha/2} s_\varepsilon \sqrt{\frac{\bar{x}^2}{S_{xx}}} \qquad (13)$$

To determine a 95% confidence interval in both cases, alpha will equal 0.05. The degrees of freedom necessary to find the t-value is 23.

The sample correlation coefficients are calculated for each scatterplot. The correlation coefficient indicates the strength of the linear relation between the x-values (buoy) and the y-values (TRMM). The equation for the sample correlation is:

$$r_{yx} = \frac{S_{xy}}{\sqrt{S_{xx} S_{yy}}} \qquad (14)$$

where

$$S_{yy} = \sum_i (y_i - \bar{y})^2 \qquad (15)$$

Overall the sample correlation coefficient will be positive if y increases as x increases. The average error of the sample correlation coefficient is given by:

$$\sigma_r = \frac{1 - r^2}{\sqrt{n}}, \qquad (16)$$

where n represents sample size.

CHAPTER VI

RESULTS

6.1 OVERLAP Subset

FIG. 3 shows the mean rain rate from TRMM versus the rain rates for each buoy. Rain rates range from 0.002 mm hr^{-1} (17.52 mm yr^{-1}) to 0.424 mm hr^{-1} (3714.24 mm yr^{-1}). The OVERLAP mean rain rate data can be found in Appendix B. The OVERLAP mean data set gives very high correlation coefficients and low average errors for the TMI, PR and COMB cases (FIG. 3) . The correlation coefficient values are around 0.9 for all three cases. The null hypothesis in this case is that the buoy and TRMM rain rates are equal. The TMI versus buoy's 95% confidence interval on the slope contains 1.0 (TABLE 2) which indicates that the null hypothesis cannot be rejected at this level for the TMI. The confidence intervals on the slope for the PR and COMB do not contain 1.0. The null hypotheses is rejected for the PR and COMB at the 95% level.

6.2 MATCH Subset

Due to the smaller sample size, the scatter of the MATCH subset is greater than for the OVERLAP subset (FIG. 4). Rain rates range from -0.014 mm hr^{-1} (-122.64 mm yr^{-1}) to 0.621 mm hr^{-1} (5439.96 mm yr^{-1}). The MATCH mean rain rate data can be found in Appendix B. The TMI versus buoy case has a 0.93 correlation coefficient. The MATCH subset also gives high correlation coefficients for both the PR and COMB cases, although these coefficients are lower than for the OVERLAP subset. The

correlation coefficient values are 0.80 and 0.79, respectively. Another significant finding is that the TMI's 95% confidence interval on the slope contains 1.0 (TABLE 2). Since the null hypothesis is the same as in the OVERLAP subset, it is not rejected for the TMI case. The confidence interval on the slope from the PR and COMB product do not contain 1.0, therefore, the null hypothesis is rejected for the PR and COMB products at the 95% level.

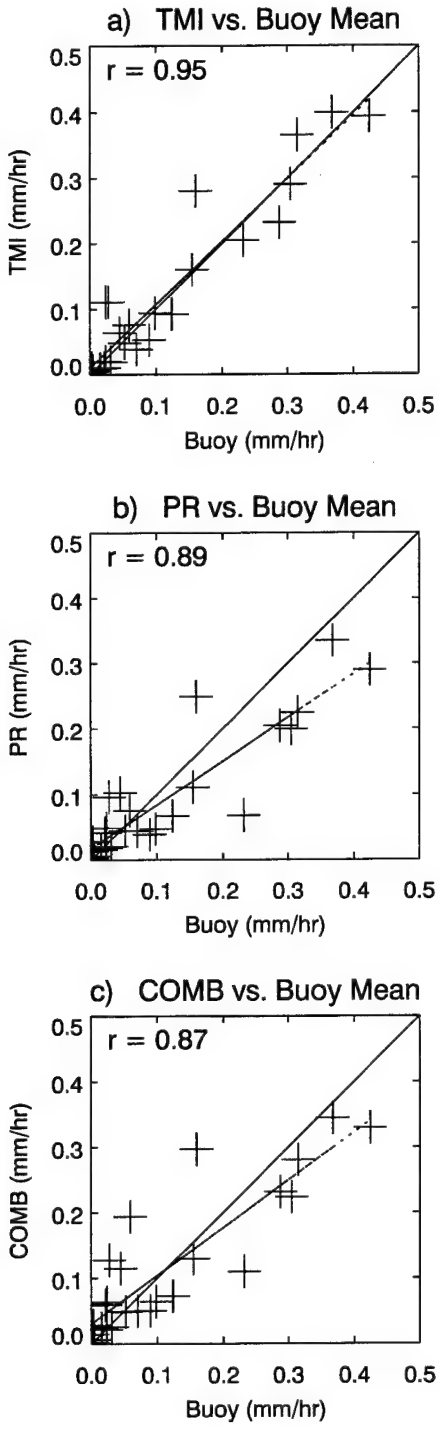

FIG. 3. Scatterplots of OVERLAP (a) TMI mean rainfall rate (mm hr $^{-1}$; ordinate) vs. buoy mean rainfall rate (mm hr $^{-1}$; abscissa); (b) as in (a), but PR mean rainfall rate vs. buoy mean rainfall rate; (c) as in (a), but COMB mean rainfall rate vs. buoy mean rainfall rate. The dotted line represents the best-fit line.

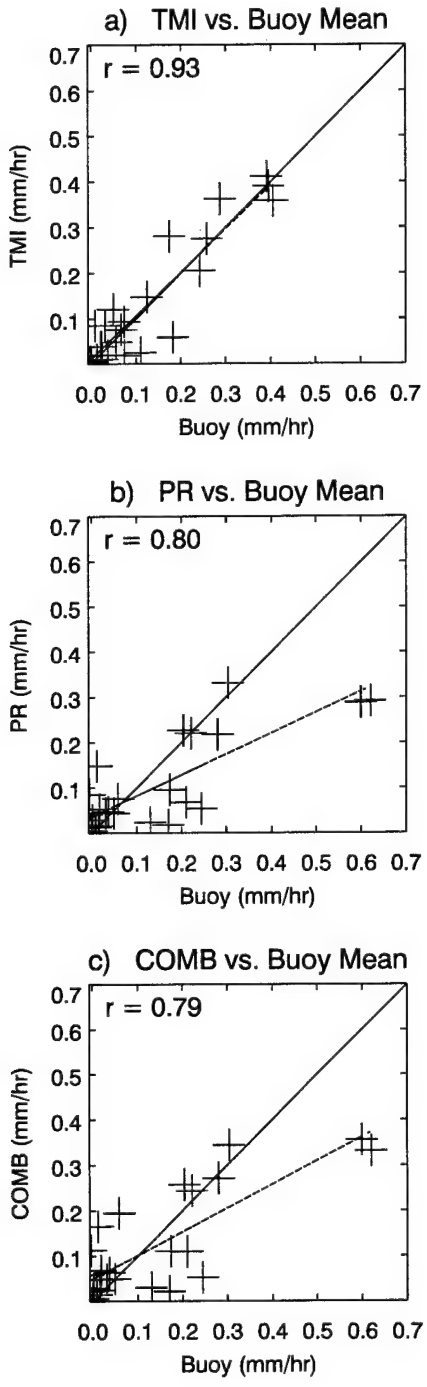

FIG. 4. Same as in FIG. 3, but for the MATCH subset.

TABLE 2. Statistics information for the OVERLAP and MATCH subsets.

	r	Avg error of r	Sample Standard Deviation	Slope	95% CI on Slope	Intercept	95% CI on Intercept
OVERLAP MEAN PLOTS							
TMI vs Buoy	.95	0.01	0.084	0.96	(0.83, 1.10)	0.01	(-1.11, 1.14)
PR vs Buoy	.89	0.02	0.089	0.66	(0.52, 0.81)	0.02	(-1.11, 1.14)
COMB vs Buoy	.87	0.03	0.109	0.73	(0.55, 0.91)	0.03	(-1.09, 1.16)
MATCH MEAN PLOTS							
TMI vs Buoy	.93	0.01	0.103	.957	(0.79, 1.12)	0.01	(-1.08, 1.10)
PR vs Buoy	.80	0.04	0.126	.46	(0.31, 0.61)	0.04	(-0.85, 0.92)
COMB vs Buoy	.79	0.04	0.145	.521	(0.35, 0.70)	0.05	(-0.83, 0.93)

CHAPTER VII

SUMMARY AND CONCLUSIONS

The purpose of this ground truth study was to determine how well TRMM-observed rain rates compared to buoy rain rate measurements. The buoy measurements were taken as ground truth. The TMI, PR and COMB rain rate products from TRMM were compared with buoy rain rate measurements from capacitance-type rain gauges on board the Next Generation ATLAS buoys. The rain rates were matched into 10-minute windows. TRMM data were averaged over 1.0° x 1.0° boxes centered on twenty-five different buoy locations across the Pacific Ocean.

This study looked at data from a four-year period beginning in January of 1998 and ending in December of 2001. All rain rate measurements from both TRMM and the buoy data sets comprise the OVERLAP subset of data. All of the mean rain rate measurements from the OVERLAP time period were statistically compared to one another. Then, all rain rate measurements that were observed at the same time by both the buoy and TRMM were used as a second source of data comparison (MATCH subset).

The mean rain rates for the OVERLAP and MATCH time periods were plotted against each other: TMI versus buoy, PR versus buoy, and COMB versus buoy. The best fit line, correlation coefficient, and the 95% confidence intervals on the slopes were calculated for each case. The confidence interval on the slope for the TMI versus buoy case in the OVERLAP and MATCH subset contained the value of one. From this observation, it is concluded that the TMI rain rate measurements showed no bias as

compared to the buoy rain rate measurements. The PR and COMB cases underestimated rain rates as compared to the buoy rain rate measurements.

REFERENCES

Chang, A. T. C. , L. S. Chiu, and T. T. Wilheit, 1993: Oceanic monthly rainfall derived from SSM/I. *Eos, Trans. Amer. Geophys. Union.*, **74**, 505-513.

Haddad, Z. S., E. A. Smith, C. D. Kummerow, T. Iguchi, M. R. Farrar, S. L. Durden, M. Alves, and W. S. Olson, 1997: The TRMM 'day-1' radar/radiometer combined rain-profiling algorithm. *Journal of the Meteorological Society of Japan*, **75**, 799-808.

Hitschfeld, W., and J. Bordan, 1954: Errors inherent in the radar measurement of rainfall at attenuating wavelengths. *J. Meteor.*, **11**, 58-67.

Iguchi, T., and R. Meneghini, 1994: Intercomparison of single-frequency methods for retrieving a vertical rain profile from airborne or spaceborne radar data. *J. Atmos. Oceanic Technol.*, **11**, 1507-1516.

Iguchi, T., T. Kozu, R. Meneghini, J. Awaka, K. Okamoto, 2000: Rain-profiling algorithm for the TRMM Precipitation Radar. *J. Appl. Meteor.*, **39**, 2038-2052.

Kummerow, C., 1993: On the accuracy of the Eddington approximation for radiative transfer in the microwave frequencies. *J. Geophys. Res.*, **98**, 2757-2765.

Kummerow, C., W. S. Olson, and L. Giglio, 1996: A simplified scheme for obtaining precipitation and vertical hydrometeor profiles from passive microwave sensors. *IEEE Trans. Geosci. Remote Sens.*, **34**, 1213-1232.

Kummerow, C. D., W. Barnes, T. Kozu, J. Shiue, and J. Simpson, 1998: The Tropical Rainfall Measuring Mission (TRMM) sensor package. *J. Atmos. Ocean. Tech.*, **15**. 809-817.

Kummerow, C. D., D. –B. Shin, Y. Hong, W. S. Olson, S. Yang, R. F. Adler, J. McCollum, R. Ferraro, G. Petty and T. T. Wilheit, 2001: The evolution of the Goddard Profiling Algorithm (GPROF) for rainfall estimation from passive microwave sensors. *J. Appl. Meteor.*, **40**, 1801-1820.

Meneghini, R., and T. Kozu, 1990: *Spaceborne Weather Radar*. Artech House, 199 pp.

Nespor, V. and B. Sevruk, 1999: Estimation of wind-induced error of rainfall gauge measurements using a numerical simulation. *J. Atmos. Oceanic Technol.*, **16**, 450-464.

Nystuen, J. A., 1999: Relative performance of automatic rain gauges under different rainfall conditions. *J. Atmos. Oceanic Technol.*, **16**, 1025-1043.

Olson, W. S., Y. Hong, C. D. Kummerow, and J. Turk, 2001: A texture-polarization method for estimating convective-stratiform precipitation area coverage from passive microwave radiometer data. *J. Appl. Meteor.*, **40**, 1577-1591.

Ott, R. L., and M. Longnecker, 2001: *An Introduction to Statistical Methods and Data Analysis*. Wadsworth Group, 1152 pp.

Petty, G. W., 1994: Physical retrievals of over-ocean rain rate from multichannel microwave imager. Part I: Theoretical characteristics of normalized polarization and scattering indices. *Meteor. Atmos. Phys.*, **54**, 79-99.

Roberti, L., J. Haferman, and C. Kummerow, 1994: Microwave radiative transfer through horizontally inhomogeneous precipitating clouds. *J. Geophys. Res.*, **99**, 16707-16718.

Rudolf, B., H. Hauschild, W. Ruth, and U. Schneider, 1996: Comparison of raingauge analyses, satellite-based precipitation estimates, and forecast model results. *Adv. Space Res.*, **18**, 53-62.

Serra, Y. L., P. A'Hearn, H. P. Freitag, and M. J. McPhaden, 2001: ATLAS self-siphoning rain gauge error estimates. *J. Atmos. Ocean. Tech.*, **18**, 1989-2002.

Serra, Y. L. and M. J. McPhaden, 2002: Multiple Time and Space Scale Comparisons of ATLAS Buoy Rain Gauge Measurements to TRMM Satellite Precipitation Measurements. Submitted to *J. Appl. Meteor.*

Thiele, O. W., M. J. McPhaden, and D. A. Short, 1995: Optical rain gauge performance. *Proc. of the Second Workshop on Optical Rain Gauge Measurements*, Greenbelt, MD, NASA, 76 pp.

Viltard, N., C. Kummerow, W. S. Olson, and Y. Hong, 2000: Combined use of the radar and radiometer of TRMM to estimate the influence of drop size distribution on rain retrievals. *J. Appl. Meteor.*, **39**, 2103-2114.

Wilheit, T. T., A. Chang, and L. Chiu, 1991: Retrieval of monthly rainfall indices from microwave radiometric measurements using probability density function. *J. Atmos. Oceanic Technol.*, **8**, 118-136.

APPENDIX A

ACRONYMS AND ABBREVIATIONS

ABBREVIATION	DEFINITION
ATLAS	Autonomous Temperature Line Acquisition System
COADS	Comprehensive Ocean-Atmosphere Data Set
dB	decibels
DMSP	Defense Meteorological Satellite Program
DSD	Drop-size distribution
ESMR	Electrically Scanning Microwave Radiometer
GCE	Goddard cumulus ensemble
GMT	Greenwich Mean Time
GPCC	Global Precipitation Climatology Centre
GPROF	Goddard profiling algorithm
GTS	Global Telecommunications System
IR	Infrared
NASA	National Aeronautics and Space Administration
NASDA	National Space Development Agency
NCLW	non-precipitating cloud liquid water
NESDIS	National Environmental Satellite, Data, and Information Service
NOAA	National Oceanic and Atmospheric Administration
PIA	path-integration attenuation

ABBREVIATION	DEFINITION
PMEL	Pacific Marine Environmental Laboratory
PR	Precipitation Radar
SSM/I	Special Sensor Microwave/Imager
TAO/TRITON	Tropical Atmosphere-Ocean/Triangle Trans-Ocean Buoy Network
TMI	TRMM Microwave Imager
TOGA COARE	Tropical Ocean Global Atmosphere Coupled Ocean Atmosphere Response Experiment
TRMM	Tropical Rainfall Measuring Mission
TSDIS	TRMM Science Data and Information System
VIRS	Visible and Infrared Radiometer System

APPENDIX B

RAIN RATE TABLES

TABLE 3. Mean rain rate data (mm hr^{-1}) plotted in FIG. 3.

Latitude	Longitude	Buoy	TMI	PR	COMB
0°N	110°W	.003	.004	.027	.028
0°N	125°W	.024	.110	.049	.063
0°N	140°W	.005	.006	.005	.007
0°N	165°E	.089	.052	.039	.050
0°N	170°W	.021	.010	.04	.059
0°N	180°W	.031	.019	.02	.026
0°N	95°W	.015	.009	.016	.024
2°N	140°W	.023	.019	.018	.022
2°N	165°E	.154	.160	.111	.130
2°N	95°W	.052	.048	.044	.048
2°S	140°W	.002	.001	.003	.002
2°S	165°E	.124	.092	.067	.072
2°S	95°W	.045	.063	.102	.114
5°N	140°W	.098	.094	.048	.064
5°N	165°E	.315	.366	.224	.28
5°N	95°W	.232	.205	.068	.11
5°S	140°W	.07	.038	.044	.05
5°S	165°E	.288	.232	.204	.231
5°S	95°W	.028	.110	.096	.127
8°N	125°W	.002	.010	.013	.015
8°N	165°E	.304	.291	.199	.223
8°N	95°W	.160	.281	.249	.297
8°S	165°E	.368	.40	.334	.345
8°S	95°W	.059	.075	.076	.194
9°N	140°W	.424	.394	.29	.33

TABLE 4. Mean rain rate data (mm hr^{-1}) plotted in FIG. 4.

		MATCH TMI		MATCH PR		MATCH COMB	
Latitude	**Longitude**	**Buoy**	**TMI**	**Buoy**	**PR**	**Buoy**	**COMB**
0°N	110°W	.005	.004	.002	.029	.002	.029
0°N	125°W	.050	.121	.018	.053	.018	.068
0°N	140°W	-.001	.005	.001	.005	.001	.006
0°N	165°E	.110	.025	.13	.024	.13	.03
0°N	170°W	-.014	.010	-.011	.042	-.011	.059
0°N	180°W	.038	.02	-.009	.018	-.009	.023
0°N	95°W	.014	.009	.016	.016	.016	.025
2°N	140°W	.074	.02	.17	.018	.17	.022
2°N	165°E	.124	.148	.17	.096	.173	.111
2°N	95°W	.056	.048	.032	.045	.032	.048
2°S	140°W	-.001	.001	.001	.003	.001	.002
2°S	165°E	.182	.058	.245	.054	.245	.053
2°S	95°W	.032	.084	.012	.148	.012	.166
5°N	140°W	.074	.093	.037	.047	.037	.063
5°N	165°E	.287	.362	.281	.217	.281	.271
5°N	95°W	.242	.205	.210	.068	.210	.11
5°S	140°W	.023	.038	.05	.044	.05	.05
5°S	165°E	.174	.281	.204	.227	.20	.257
5°S	95°W	.01	.084	-.004	.086	-.004	.113
8°N	125°W	.026	.010	.009	.013	.009	.015
8°N	165°E	.258	.275	.221	.22	.221	.244
8°N	95°W	.405	.358	.60	.288	.6	.356
8°S	165°E	.391	.411	.304	.332	.304	.344
8°S	95°W	.067	.076	.059	.076	.059	.195
9°N	140°W	.395	.390	.621	.292	.621	.332

VITA

Amy Blackmore Phillips was born in Minot, North Dakota on [redacted]. She graduated from Central High School in Grand Forks, North Dakota in May of 1994. In May of 1998, she graduated from the University of Missouri with a Bachelor of Science in soil and atmospheric sciences and was commissioned as a Second Lieutenant in the United States Air Force. After serving with the 46th Weather Squadron at Eglin Air Force Base, Florida, she received her Master of Science degree from the Atmospheric Sciences Department at Texas A&M through the Air Force Institute of Technology Civilian Institute program. Captain Phillips is currently assigned to the 28th Operational Weather Squadron at Shaw Air Force Base in Sumter, South Carolina.

Correspondence may be directed to:

[redacted]